

# Orientation-dependent indentation response of helium-implanted tungsten <sup>EP</sup>

Cite as: Appl. Phys. Lett. **114**, 221905 (2019); <https://doi.org/10.1063/1.5097403>

Submitted: 25 March 2019 . Accepted: 07 May 2019 . Published Online: 06 June 2019

Suchandrima Das <sup>id</sup>, Hongbing Yu <sup>id</sup>, Edmund Tarleton <sup>id</sup>, and Felix Hofmann <sup>id</sup>

## COLLECTIONS

<sup>EP</sup> This paper was selected as an Editor's Pick



View Online



Export Citation



CrossMark

## ARTICLES YOU MAY BE INTERESTED IN

Large superelastic recovery and elastocaloric effect in as-deposited additive manufactured Ni<sub>50.8</sub>Ti<sub>49.2</sub> alloy

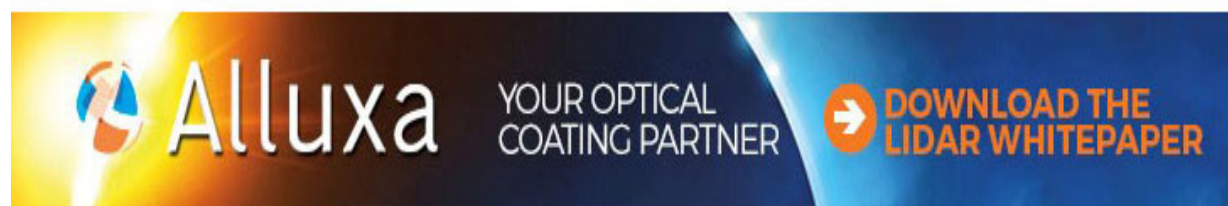
Applied Physics Letters **114**, 221903 (2019); <https://doi.org/10.1063/1.5098371>

Growth and fabrication of GaN/Er:GaN/GaN core-cladding planar waveguides

Applied Physics Letters **114**, 222105 (2019); <https://doi.org/10.1063/1.5093942>

Tuning the electronic properties of epitaxial strained CaFeO<sub>3-δ</sub> thin films

Applied Physics Letters **114**, 221907 (2019); <https://doi.org/10.1063/1.5098025>



# Orientation-dependent indentation response of helium-implanted tungsten

Cite as: Appl. Phys. Lett. **114**, 221905 (2019); doi: [10.1063/1.5097403](https://doi.org/10.1063/1.5097403)

Submitted: 25 March 2019 · Accepted: 7 May 2019 ·

Published Online: 6 June 2019



View Online



Export Citation



CrossMark

Suchandrima Das,<sup>1,a)</sup>  Hongbing Yu,<sup>1</sup>  Edmund Tarleton,<sup>2</sup>  and Felix Hofmann<sup>1,b)</sup> 

## AFFILIATIONS

<sup>1</sup>Department of Engineering Science, University of Oxford, Oxford OX1 3PJ, United Kingdom

<sup>2</sup>Department of Materials, University of Oxford, Oxford OX1 3PH, United Kingdom

<sup>a)</sup>[suchandrima.das@eng.ox.ac.uk](mailto:suchandrima.das@eng.ox.ac.uk)

<sup>b)</sup>[felix.hofmann@eng.ox.ac.uk](mailto:felix.hofmann@eng.ox.ac.uk)

## ABSTRACT

A literature review of studies investigating the topography of nano-indents in ion-implanted materials reveals seemingly inconsistent observations, with reports of both pile-up and sink-in. This may be due to the crystallographic orientation of the measured sample point, which is often not considered when evaluating implantation-induced changes in the deformation response. Here, we explore the orientation dependence of spherical nano-indentation in pure and helium-implanted tungsten, considering grains with  $\langle 001 \rangle$ ,  $\langle 110 \rangle$ , and  $\langle 111 \rangle$  out-of-plane orientations. Atomic force microscopy of indents in unimplanted tungsten shows little orientation dependence. However, in the implanted material, a much larger, more localized pile-up is observed for  $\langle 001 \rangle$  grains than for  $\langle 110 \rangle$  and  $\langle 111 \rangle$  orientations. Based on the observations for  $\langle 001 \rangle$  grains, we hypothesize that a large initial hardening due to helium-induced defects is followed by localized defect removal and subsequent strain softening. A crystal plasticity finite element model of the indentation process, formulated based on this hypothesis, accurately reproduces the experimentally observed orientation-dependence of the indent morphology. The results suggest that the mechanism governing the interaction of helium-induced defects with glide dislocations is orientation independent. Rather, differences in the pile-up morphology are due to the relative orientations of the crystal slip systems, sample surface, and spherical indenter. This highlights the importance of accounting for crystallographic orientation when probing the deformation behavior of ion-implanted materials using nano-indentation.

© 2019 Author(s). All article content, except where otherwise noted, is licensed under a Creative Commons Attribution (CC BY) license (<http://creativecommons.org/licenses/by/4.0/>). <https://doi.org/10.1063/1.5097403>

Ion-implantation is commonly used to mimic irradiation damage in materials. This cost-effective technique allows examination of specific irradiation factors. For example, helium-implantation introduces irradiation like defects while enabling examination of the interaction of these defects with the implanted helium.<sup>1–3</sup> Similarly, self-ion implantation has been extensively employed to emulate the cascade damage caused by neutron irradiation.<sup>4,5</sup>

Nano-indentation is often used to gain insight into the mechanical properties of the few-micron-thick ion damaged layers. Marked changes in the pile-up morphology around nano-indents have been observed in irradiated materials, even for low damage levels. A review of several studies reveals seemingly contradictory observations. For example, large pile-up around 250 nm deep Berkovich nano-indents was observed in 0.3 at. % helium-implanted W-1 at. % Re.<sup>6</sup> But for HT9 ferritic/martensitic steel, implanted with both helium and protons, there was no noticeable difference in the indent surface profile.<sup>7</sup> A suppression of pile-up was noticed around indents in 2 MeV W<sup>+</sup> ion implanted W-5 wt.

%Ta (0.04 dpa).<sup>8</sup> On the other hand, Fe<sup>+</sup> implantation of Fe-12 wt. %Cr leads to a distinct increase in pile-up.<sup>9</sup>

This raises the question why implantation with helium or self-ions causes a pile-up increase in some materials and suppression in others. Generally, pile-up and sink-in are associated with low and high strain-hardening potential, respectively.<sup>10,11</sup> Different annealing conditions could lead to differences in strain-hardening potential and consequently different surface profiles. Interestingly, nano-indentation in annealed single crystals has shown a strong dependence of the deformation pattern on the crystallographic orientation of the crystal.<sup>12–14</sup> This was also seen in atomistic simulations concentrating on the early stages of nano-indentation in fcc crystals.<sup>15</sup>

In most nano-indentation studies of ion-implanted material, crystallographic orientation is not considered. This raises the question whether the pile-up morphology and consequently the measured hardness may be orientation-dependent. If this is the case, then conclusions drawn from indentation of material with unknown crystal orientation could be misleading.

Here, we concentrate on tungsten, the main candidate material for fusion reactor armor due to its high melting point (3422 °C) and strength at high temperature.<sup>16–18</sup> Helium-defects are known to cause substantial property changes in tungsten, e.g., increased hardness,<sup>19</sup> lattice swelling,<sup>1–3</sup> and reduced thermal diffusivity.<sup>20</sup> Recently, comparing spherical nano-indents in 0.3 at. % helium-implanted and unimplanted parts of the same tungsten  $\langle 001 \rangle$  single crystal, we found a large, localized increase in pile-up around indents in the helium-implanted material.<sup>21</sup> Here, we examine whether this helium-induced change in the pile-up morphology is dependent on grain orientation. For each crystal orientation, besides the indent surface morphology, the deformation field beneath specific indents is investigated using a physically based crystal plasticity finite element (CPFE) model.

A tungsten poly-crystal (99.99% purity,  $\sim 180 \mu\text{m}$  grain size) was recrystallised in vacuum at 1400 °C. The surface was mechanically ground and then polished using diamond paste. Final chemo-mechanical polishing with 0.1  $\mu\text{m}$  colloidal silica suspension produced a high quality surface finish. Part of the sample was implanted with helium at the National Ion Beam Centre, University of Surrey, UK. Implantation was performed at 298 K using a 2 MeV ion accelerator and a raster scanned beam to ensure a uniform implantation dose. The implantation profile, estimated using SRIM<sup>22</sup> (displacement energy of 68 eV, single-layer calculation model<sup>23</sup>) is provided in Appendix A of the [supplementary material](#). Using a combination of different ion energies and fluences (Appendix B, the [supplementary material](#)), an almost uniform helium ion concentration  $>3000$  appm (associated damage of  $\sim 0.24$  dpa) was obtained within an  $\sim 2.8 \mu\text{m}$  thick implanted layer. Frenkel pair formation is likely to be the main damage mechanism as helium-implantation-induced recoils have predominantly low energy.<sup>2</sup> Little defect clustering is expected given that vacancies in tungsten have low mobility at room temperature.<sup>24–26</sup>

Using electron back-scatter diffraction (EBSD), grains with near  $\langle 001 \rangle$ ,  $\langle 110 \rangle$ , and  $\langle 111 \rangle$  orientations were selected in both the unimplanted and implanted regions of the sample.

The out-of-plane orientations of the twelve selected grains and their misorientation with respect to the perfect  $\langle 111 \rangle$ ,  $\langle 110 \rangle$ , or  $\langle 001 \rangle$  out-of-plane direction are shown in Table C.1 in Appendix C of the [supplementary material](#).

Four 500 nm deep spherical nano-indents were made for each orientation for both implanted and unimplanted areas (MTS NanoXp, Synton  $\sim 5 \mu\text{m}$  radius diamond tip, 50  $\mu\text{m}$  spacing between indents). The use of a spherical indenter tip removes the additional complexity of in-plane indenter orientation relative to the crystal associated with non-rotationally symmetric tips, e.g., Berkovich. SEM micrographs (Zeiss Merlin FEG SEM) of the nano-indents in  $\langle 111 \rangle$ ,  $\langle 001 \rangle$ , and  $\langle 110 \rangle$  grains in the helium-implanted and unimplanted material are shown in Appendix D, the [supplementary material](#). They clearly show that consistent results are obtained across the indents for each crystal orientation.

To quantify the pile-up morphology, atomic force microscopy (AFM) was carried out on one indent per grain orientation in the implanted and unimplanted material (Fig. 1). AFM measurements were performed in the contact mode using a Digital Instruments Dimension 3100 AFM with Bruker CONTV-A tips (10 nm nominal tip radius). Little difference is seen between indents in different grains of the unimplanted sample [Figs. 1(d)–1(f)]. However, in the implanted samples, there are striking orientation-dependent variations

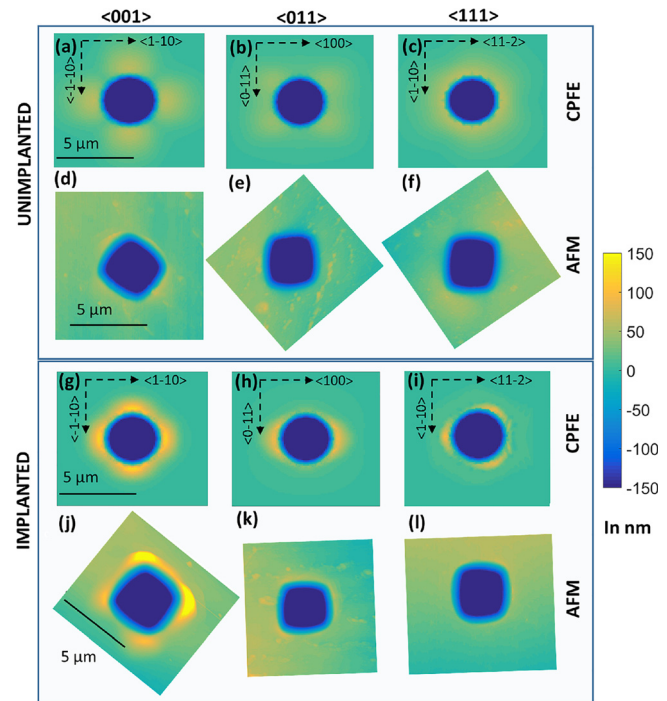


**FIG. 1.** Surface profiles of residual out-of-plane displacement after indentation. CPFE simulations for the unimplanted (a)–(c) and the helium-implanted sample (g)–(i) for  $\langle 001 \rangle$ ,  $\langle 011 \rangle$ , and  $\langle 111 \rangle$  out-of-plane crystal orientations, respectively. AFM for the unimplanted (d)–(f) and the helium-implanted sample (j)–(l) for  $\langle 001 \rangle$ ,  $\langle 011 \rangle$ , and  $\langle 111 \rangle$  out-of-plane crystal orientations, respectively. The AFM micrographs have been rotated to match the in-plane orientations as labeled on the CPFE plots. The color scale and 5  $\mu\text{m}$  scale bar are the same for all plots. Although the indent depth below the surface, after unloading, is  $\sim 400$  nm, a color-scale of  $-150$  to  $150$  nm is used as we concentrate on investigating the pile-up morphology on the sample surface.

in the pile-up morphology [Figs. 1(j)–1(l)]. The  $\langle 001 \rangle$  grain shows the characteristic large pile-up and distinct slip steps we previously observed.<sup>21</sup> Surprisingly, indents in  $\langle 011 \rangle$  and  $\langle 111 \rangle$  grains, though in the same polycrystalline implanted sample, show very little pile-up. Indeed, comparing AFM measurements of indents in  $\langle 011 \rangle$  and  $\langle 111 \rangle$  grains of the unimplanted and helium-implanted material could lead to the incorrect conclusion that helium does not significantly modify the deformation behavior of tungsten.

Orientation-dependent differences are also seen in the load-displacement curves shown in Fig. 2. Each curve is the average load-displacement response recorded from the four indents per orientation. In the unimplanted grains, there is little difference between the different crystal orientations. In the helium-implanted material, on the other hand, the load for the  $\langle 001 \rangle$  orientation is  $\sim 20\%$  higher than for  $\langle 011 \rangle$  and  $\sim 30\%$  higher than for  $\langle 111 \rangle$ .

To explore the origin of the orientation-dependence of indentation behavior in the helium-implanted material, we consider a CPFE model of the indentation process. Recently, we developed a CPFE formulation to simulate nano-indentation of a helium-implanted  $\langle 001 \rangle$  oriented tungsten single crystal.<sup>27</sup> The formulation is based on a hypothesis derived from a comparative study of nano-indentation and microbeam Laue diffraction measurements performed on helium-

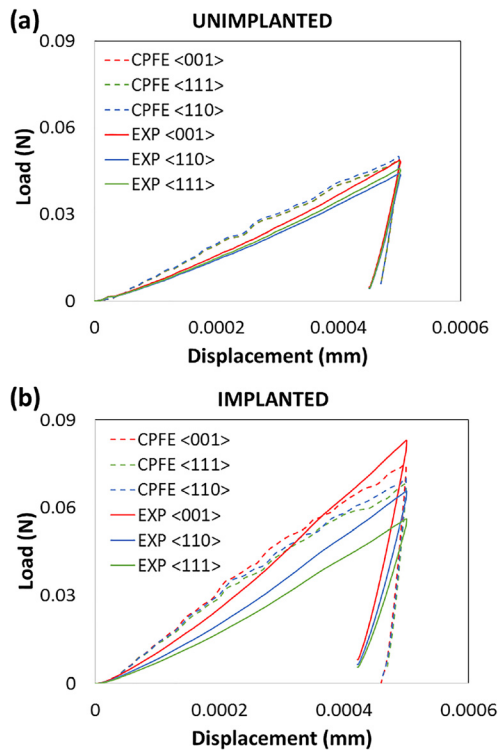


**FIG. 2.** Load vs displacement curves of the (a) unimplanted sample and (b) helium-implanted sample for the  $\langle 001 \rangle$ ,  $\langle 011 \rangle$ , and  $\langle 111 \rangle$  from the nano-indentation experiment and CPFE simulation superimposed. The solid curves, i.e., those measured from nano-indentation experiments, are the average of four measurements performed on four different indents.

implanted and unimplanted parts of a tungsten  $\langle 001 \rangle$  crystal.<sup>21</sup> Here, we use the same CPFE formulation with the appropriate orientation matrix to simulate indentation of the  $\langle 011 \rangle$  and  $\langle 111 \rangle$  grain of the polycrystalline tungsten sample. All other parameters of the model were kept constant. Below, we briefly discuss the model and the underlying hypothesis. Further details can be found elsewhere.<sup>27</sup>

Microbeam Laue diffraction measurements of the deformation zone beneath indents in a  $\langle 001 \rangle$  single crystal showed a more tightly confined plastic zone in the helium-implanted sample than in the unimplanted material.<sup>21</sup> Increased pile-up, slip steps, and increased indentation load were observed in the implanted material. Based on these observations, we hypothesized the following mechanism for the interaction of glide dislocations and helium-implantation-induced defects (known to consist predominantly of Frenkel pairs that cannot recombine as helium occupies the vacancy<sup>2</sup>). We propose that initially, helium-defects strongly obstruct gliding dislocations and cause a pronounced hardening. However, with progressive deformation, passing dislocations facilitate the release of helium from the defect cluster and consequently recombination of Frenkel pairs. Reduced defect density channels are thus formed that allow easier propagation of subsequent dislocations. This leads to a localisation of deformation, which in turn is the origin of the large pile-up and slip steps observed for the  $\langle 001 \rangle$  orientation. A model based on this hypothesis was implemented in a CPFE user material subroutine (UMAT) for Abaqus where strain softening was applied to the helium-implanted layer.

The UMAT is based on a user-element developed by Dunne *et al.*<sup>28</sup> and is founded on the theory of multiplicative decomposition of the deformation gradient into elastic and plastic components.<sup>29,30</sup> Briefly, the CPFE formulation constrains slip to applicable slip-systems (assumed to be the 12  $\{110\}$  slip planes with  $a/2 \langle 111 \rangle$  slip vector directions<sup>31</sup>). The slip rate is governed by a physically based constitutive law that considers the glide of thermally activated dislocations in a field of pinning obstacles.<sup>28</sup> Taylor hardening is implemented, where the critically resolved shear stress (CRSS), with initial value  $\tau_c^0$ , is increased as a function of evolving densities of geometrically necessary dislocations (GNDs).<sup>32</sup> The CRSS in the unimplanted sample is  $\tau_c = \tau_c^0 + CGb\sqrt{\rho_{\text{GND}}}$ , where  $G$  is the shear modulus of tungsten,  $b$  the Burgers vector, and  $\rho_{\text{GND}}$  the sum of the GNDs produced across all slip-systems. A modified form of this equation is used in the helium-layer;  $\tau_c = \tau_c^0 + CGb\sqrt{\rho_{\text{GND}}} + \tau_H$ , where the additional  $\tau_H$  term accounts for the increased resistance to the dislocation glide due to helium-defects. To account for the strain softening,  $\tau_H$  is reduced at the end of each time increment,  $\Delta t$ , if the material point was deformed plastically. The reduction in  $\tau_H$  represents the gradual formation of defect-free regions and consequently easier dislocation glide.  $\tau_H$  is considered to be a function of the total accumulated crystallographic slip and the rate at which it decreases is estimated to be proportional to its current value, i.e., the current helium-defect concentration ( $\frac{\partial \tau_H}{\partial \beta_p} \big|_{t+\Delta t} = -\tau_H/\gamma$ ). This suggests an exponential softening

$$\tau_H^{t+\Delta t} = \tau_H^0 e^{-(\beta_p^{t+\Delta t}/\gamma)}, \quad (1)$$

$$\beta_p^{t+\Delta t} = \beta_p^t + \sum_{\lambda=1}^n \dot{\beta}_p^{\lambda} \Delta t, \quad (2)$$

where  $\dot{\beta}_p^{\lambda}$  is the crystallographic slip rate on slip system  $\lambda$ ,  $\beta_p^t$  and  $\beta_p^{t+\Delta t}$  are the total accumulated crystallographic slip, summed over all slip systems, at the start and end of the time increment, and  $\tau_H^0$  is the initial value of  $\tau_H$ . Only three UMAT parameters were fitted to the nano-indentation and AFM results of the  $\langle 001 \rangle$  grain: the initial unimplanted CRSS,  $\tau_c^0$ , the hardening prefactor  $C$ , and only one additional parameter for the helium-layer, the softening-rate  $\gamma$ . All other UMAT parameters, including  $\tau_H^0$ , were physically derived or taken from literature values.<sup>27</sup>

The geometry for CPFE simulations was a 3D,  $20 \times 20 \times 20 \mu\text{m}^3$  sample block and a  $5 \mu\text{m}$  radius spherical indenter simulated in Abaqus 2016 (Dassault Systèmes, Providence, RI, USA). Based on symmetry, for the  $\langle 001 \rangle$  and  $\langle 011 \rangle$  grains, the model simulated one quarter of the experimental setup. For the  $\langle 111 \rangle$  grain, a model simulating a third of the experimental setup was used. The boundary conditions applied to the indentation model in Abaqus included symmetric XZ and YZ planes, a traction free top surface, and fixed displacement and rotation boundary conditions on the remaining surfaces.

The  $20 \mu\text{m}$  high block was partitioned into two layers: a  $3 \mu\text{m}$  thick top layer and a  $17 \mu\text{m}$  thick bottom layer. When simulating indentation on the helium-implanted tungsten, the top layer was assigned material parameters of implanted tungsten and the bottom layer those of pure tungsten. Additional boundary conditions,  $\sigma_{xx}^{BC} = \sigma_{yy}^{BC} = -260 \text{ MPa}$ , were applied to the helium-implanted layer to account for helium-implantation induced residual stresses. These stresses arise out of the need to maintain geometrical continuity between the implanted layer and substrate.<sup>1</sup> Derivation of these stress boundary conditions is given in Appendix E of the [supplementary material](#).



The indenter was subjected to a displacement of  $0.5\ \mu\text{m}$  into the sample block. The contact surface between the sample block and the indenter tip was assumed to be frictionless as a previous study<sup>33</sup> showed that the mechanical behavior of the substrate is not significantly affected by the coefficient of friction. A structured finite element biased mesh with  $>39\,500$  20-noded quadratic hexahedral elements with reduced integration was used (C3D20R). Figure E.1 in Appendix E of the [supplementary material](#) shows the rendered 3D mesh of the quarter model used for indentation of  $\langle 001 \rangle$  and  $\langle 011 \rangle$  oriented grains and the one-third model used for indentation of the  $\langle 111 \rangle$  oriented grain. The element size at the indent was  $50\ \text{nm}$ .

The simulated indent surface-profiles, after unloading, for both samples are shown in Fig. 1. The AFM micrographs in Fig. 1 are rotated to have the same in-plane orientation as the profiles predicted by CPFE. Four, two, and threefold symmetry can be seen in the CPFE predicted surface profiles of the  $\langle 001 \rangle$ ,  $\langle 011 \rangle$  and  $\langle 111 \rangle$  grains, respectively [Figs. 1(a)–1(c)]. The CPFE model reproduces the experimental pile-up for all three grains in the implanted sample remarkably well. In particular, the model captures the much lower pile-up in the  $\langle 011 \rangle$  and  $\langle 111 \rangle$  grains compared to the  $\langle 001 \rangle$  grain.

We note in Fig. 1 that the AFM measurements of the indent impressions are not perfectly circular. This is due to imperfections of the spherical indenter tip geometry. Flawless spherical indenter tips, especially with such a small tip radius, are difficult to manufacture. However, good agreement between the CPFE predictions (where a perfectly spherical indenter tip was simulated) and the experimental results shows that the deviations in the indent tip geometry do not significantly affect the indentation response. This is an important advantage of using a spherical indenter tip over Berkovich tips, where the sharp tip makes the indentation response very sensitive to imperfections in tip geometry.

The simulated load-displacement curves for each grain orientation in both the implanted and unimplanted samples are shown superimposed on the experimental measurements in Fig. 2. Good quantitative agreement is observed between CPFE and experimental results for the unimplanted sample. In terms of the mechanical response for the implanted samples, CPFE predictions for the  $\langle 001 \rangle$  grain reach  $\sim 14\%$  higher load than those for the  $\langle 011 \rangle$  and  $\langle 111 \rangle$  grains, with the latter two producing a very similar load response. It is important to note that the parameters of the model were determined solely based on the indentation results of the  $\langle 100 \rangle$  oriented crystal. For the simulations of the  $\langle 011 \rangle$  and  $\langle 111 \rangle$  oriented grains, all parameters except for the input crystal orientation were kept unchanged.

Anisotropy in indentation behavior has been previously noted in  $\alpha\text{-Ti}$ <sup>34</sup> and  $\text{Be}$ <sup>35</sup> polycrystals, where modulus and hardness decreased significantly with the increasing angle of inclination between the  $c$ -axis and the indentation axis. Orientation-dependent mechanical performance has been seen in tungsten too, where  $\langle 001 \rangle$  single crystals were found to be the best performing kinetic energy penetrators, owing to favorable slip during loading and shear localization.<sup>36</sup> It is interesting that orientation-dependent differences in indentation response are as pronounced at the nanoscale. The results highlight the importance of determining the crystallographic orientation of the ion-implanted sample for accurate evaluation of the ion-induced alteration in deformation behavior.

Quantitative agreement between CPFE predictions and experimental results for the implanted sample inspires some confidence in the

hypothesis that localized deformation through slip channels, formed by dislocations interacting with helium-defects, can cause the large pile-up and increased hardening. In the 1960s, Makin and Sharp proposed a mathematical theory linking the creation of large pile-up and slip-steps to an accelerating fall in the force resisting dislocation glide.<sup>37</sup> As the defect reduction rate will depend on the number density of defects, an exponential decrease in  $\tau_H$ , as implemented in the CPFE formulation in Eq. (2), is reasonable. The model uniquely captures the fourfold pile-up increase in the  $\langle 001 \rangle$  grain in the implanted samples, affirming the strain-softening hypothesis. Strain-softening and consequent slip channel formation in irradiated materials, both fcc and bcc, have been experimentally observed in numerous studies.<sup>38–40</sup> This is of particular concern as it may lead to untimely failure due to the loss of ductility.

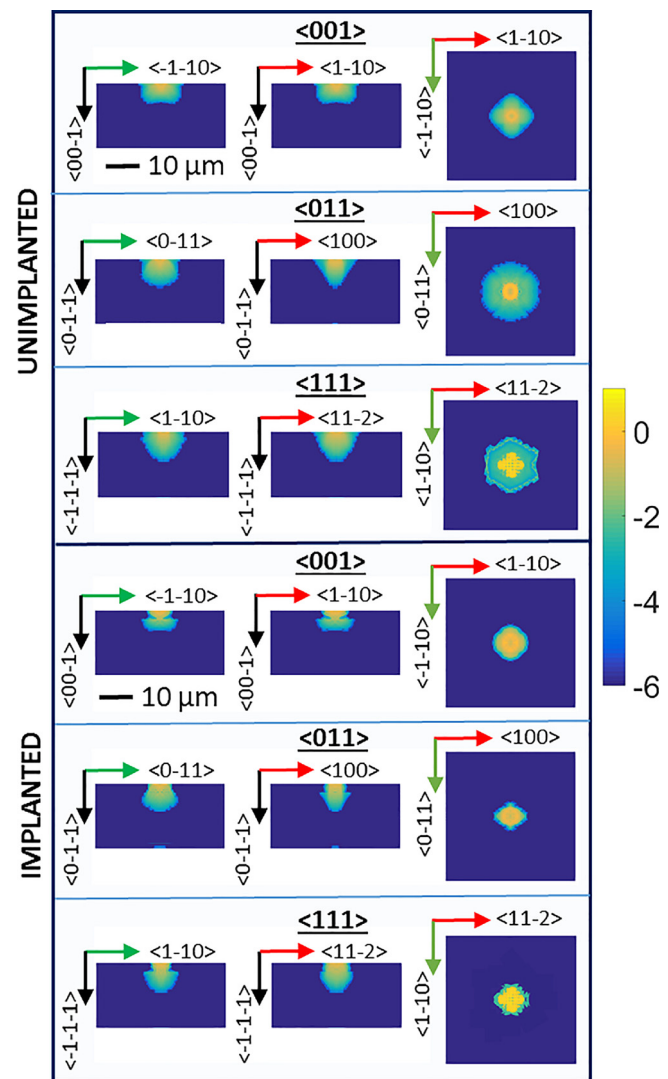


**FIG. 3.** A comparison of the effective plastic strain (on a logarithmic scale) beneath indents in all three grains for both the unimplanted sample and the helium-implanted sample as predicted by the CPFE simulation. In each case, the strain is shown on the YZ, XZ, and XY cross sections from left to right.

The CPFE predictions also provide further insight into the underlying deformation zone beneath indents. Comparison of the field of effective plastic strain beneath indents in each grain for both samples (Fig. 3) shows an orientation-independent trend. The deformation field becomes more confined near the indent in all grains in the implanted material, compared to a more widespread deformation zone in the unimplanted material.

Put together, these results suggest that the underlying mechanism responsible for the modified behavior of the implanted material, i.e., the interaction of dislocation with helium-induced defects, is orientation-independent. The changes in the pile-up morphology for different crystal orientations are simply a product of the relative orientations of the active slip systems, the indenter, and the sample surface.

In summary, we have examined the effect of helium-implantation in grains of three different orientations. It was found that (001)-oriented grains showed  $\sim 70\%$  increased hardness and  $\sim 172\%$  increased pile-up compared to unimplanted tungsten. In contrast, (011) and (111) grains show a negligible change in pile-up and only an  $\sim 30\%$  increase in hardness compared to the unimplanted sample. CPFE based on the application of strain-softening in the helium-implanted layer was able to reproduce the experimental results for all three grains with surprising accuracy. The fact that significantly different indentation behavior is observed for different grain orientations in the implanted material highlights the importance of considering crystal orientation when interpreting nano-indentation data.

See the [supplementary material](#) for the details of helium-implantation performed on the polycrystalline tungsten sample, SEM micrographs of nano-indents made in the different grains of the unimplanted and helium-implanted parts of the tungsten sample, grain orientations of the experimentally measured sample points, rendering of the finite element mesh used for the crystal plasticity simulations, and values of the material properties used in the formulation.

We thank Professor D. E. J. Armstrong for providing the sample and Dr. N. Peng for performing the ion-implantation. This work was funded by Leverhulme Trust Research Project Grant No. RPG-2016-190. Ion implantations were performed under the UK Engineering and Physical Sciences Research Council Grant No. EP/H018921/1. E.T. acknowledges financial support from the Engineering and Physical Sciences Research Council under Fellowship Grant No. EP/N007239/1.

## REFERENCES

- S. Das, W. Liu, R. Xu, and F. Hofmann, *Mater. Des.* **160**, 1226–1237 (2018).
- F. Hofmann, D. Nguyen-Manh, M. R. Gilbert, C. E. Beck, J. K. Eliason, A. A. Maznev, W. Liu, D. E. J. Armstrong, K. A. Nelson, and S. L. Dudarev, *Acta Mater.* **89**, 352–363 (2015).
- I. DeBroglie, C. E. Beck, W. Liu, and F. Hofmann, *Scr. Mater.* **107**, 96–99 (2015).
- X. Yi, M. L. Jenkins, M. A. Kirk, Z. Zhou, and S. G. Roberts, *Acta Mater.* **112**, 105–120 (2016).
- D. E. J. Armstrong, X. Yi, E. A. Marquis, and S. G. Roberts, *J. Nucl. Mater.* **432**, 428–436 (2013).
- C. E. Beck, F. Hofmann, J. K. Eliason, A. A. Maznev, K. A. Nelson, D. E. J. Armstrong, and D. E. J. Armstrong, *Scr. Mater.* **128**, 83–86 (2017).
- P. Hosemann, C. Vieh, R. R. Greco, S. Kabra, J. A. Valdez, M. J. Cappiello, and S. A. Maloy, *J. Nucl. Mater.* **389**, 239–247 (2009).
- D. E. J. Armstrong, A. J. Wilkinson, and S. G. Roberts, *Phys. Scr.* **2011**, 14076.
- C. D. Hardie, S. G. Roberts, and A. J. Bushby, *J. Nucl. Mater.* **462**, 391–401 (2015).
- W. D. Nix, *Mater. Sci. Eng., A* **234–236**, 37–44 (1997).
- C. Oliver and M. Pharr, *J. Mater. Res.* **7**, 1564–1583 (1992).
- Y. Gaillard, C. Tromas, and J. Woignard, *Acta Mater.* **51**, 1059–1065 (2003).
- D. F. Bahr, D. E. Kramer, and W. W. Gerberich, *Acta Mater.* **46**, 3605–3617 (1998).
- M. Hollatz, M. Bobeth, W. Pompe, and V. Marx, *Acta Mater.* **44**, 4149–4159 (1996).
- J. Li, K. J. Van Vliet, T. Zhu, S. Yip, and S. Suresh, *Nature* **418**, 307 (2002).
- M. Rieth, S. L. Dudarev, S. M. Gonzalez de Vicente, J. Aktaa, T. Ahlgren, S. Antusch, D. E. J. Armstrong, M. Balden, N. Baluc, M.-F. Barthe *et al.*, *J. Nucl. Mater.* **432**, 482–500 (2013).
- M. Ekman, K. Persson, and G. Grimvall, *J. Nucl. Mater.* **278**, 276–279 (2000).
- N. Wei, T. Jia, X. Zhang, T. Liu, Z. Zeng, and X. Yang, *AIP Adv.* **4**, 57103 (2014).
- D. E. J. Armstrong, P. D. Edmondson, and S. G. Roberts, *Appl. Phys. Lett.* **102**, 251901 (2013).
- F. Hofmann, D. R. Mason, J. K. Eliason, A. A. Maznev, K. A. Nelson, and S. L. Dudarev, *Sci. Rep.* **5**, 16042 (2015).
- S. Das, D. E. J. Armstrong, Y. Zayachuk, W. Liu, R. Xu, and F. Hofmann, *Scr. Mater.* **146**, 335–339 (2018).
- J. F. Ziegler and J. Biersack, *Nucl. Instrum. Methods Phys. Res., Sect. B* **268**, 1818–1823 (2010).
- ASTM E521-96, *Standard Practice for Neutron Radiation Damage Simulation by Charged-Particle Irradiation* (ASTM International, West Conshohocken, PA, USA, 2009).
- A. DeBelle, M. F. F. Barthe, and T. Sauvage, *J. Nucl. Mater.* **376**, 216–221 (2008).
- P. M. Derlet, D. Nguyen-Manh, and S. L. Dudarev, *Phys. Rev. B: Condens. Matter Mater. Phys.* **76**, 054107 (2007).
- D. Nguyen-Manh, A. P. Horsfield, and S. L. Dudarev, *Phys. Rev. B: Condens. Matter Mater. Phys.* **73**, 020101(R) (2006).
- S. Das, H. Yu, E. Tarleton, and F. Hofmann, preprint [arXiv:1901.00745](#) (2018).
- F. P. E. Dunne, D. Rugg, and A. Walker, *Int. J. Plast.* **23**, 1061–1083 (2007).
- E. H. Lee, *J. Appl. Mech.* **36**, 1–6 (1969).
- S. Das, F. Hofmann, and E. Tarleton, *Int. J. Plast.* **109**, 18–42 (2018).
- C. Marichal, H. Van Swynghevoen, S. Van Petegem, and C. Borca, *Sci. Rep.* **3**, 2547 (2013).
- G. I. Taylor, *Proc. R. Soc. A* **145**, 388–404 (1934).
- Y. Wang, D. Raabe, C. Klüber, and F. Roters, *Acta Mater.* **52**, 2229–2238 (2004).
- T. B. Britton, H. Liang, F. P. E. Dunne, and A. J. Wilkinson, *Proc. R. Soc. A* **466**, 695–719 (2010).
- V. Kuksenko, S. Roberts, and E. Tarleton, *Int. J. Plast.* **116**, 62–80 (2019).
- W. J. Bruchey, E. J. Horwath, and P. W. Kingman, in *Orientation dependence of Deformation and Penetration Behavior of Tungsten Single-Crystal Rods* (The Metallurgical Society Inc., 1991), Vol. 23, pp. 121–128.
- M. J. Makin and J. V. Sharp, *Phys. Status Solidi* **9**, 109–118 (1965).
- A. J. Bushby, S. G. Roberts, and C. D. Hardie, *J. Mater. Res.* **27**, 85–90 (2012).
- M. Victoria, N. Baluc, C. Bailat, Y. Dai, M. I. Luppó, R. Schaublin, and B. N. Singh, *J. Nucl. Mater.* **276**, 114–122 (2000).
- Y. Dai and M. Victoria, in “Defect Cluster Structure and Tensile Properties of Copper Single Crystals Irradiated With 600 MeV Protons” (MRS Online Proc. Libr. Arch., 1996), Vol. 439, p. 319.